eng

MDPI

Article

Ti-Fe-Based Alloys Modified with Al and Cr for Next-Generation Biomedical Implants

Katia Itzel Rodríguez-Escobedo [1], Wilian Jesús Pech-Rodríguez [1], Zaira Itzel Bedolla-Valdez [2,3], Carlos Adrián Calles-Arriaga [1], José Guadalupe Miranda-Hernández [4] and Enrique Rocha-Rangel [1,*]

[1] Research Department, Universidad Politécnica de Victoria, Av. Nuevas Tecnologías 5902, Parque Científico y Tecnológico de Tamaulipas, Ciudad Victoria 87138, Mexico; 2339003@upv.edu.mx (K.I.R.-E.); wpechr@upv.edu.mx (W.J.P.-R.); ccallesa@upv.edu.mx (C.A.C.-A.)
[2] Center for Applied Research, TecNM/ITS de Uruapan, Carr Uruapan-Carapan #5555, Col. La Basilia, Uruapan 60015, Mexico; zaira.bedolla@ipicyt.edu.mx
[3] Advanced Materials Division, IPICYT, Camino a la Presa de San José 2055 Col. Lomas 4a Sección, San Luis Potosí 78216, Mexico
[4] Industrial Engineering Department, Centro Universitario UAEM Valle de México, Atizapán de Zaragoza 54500, Mexico; jgmirandah@uaemex.mx
* Correspondence: erochar@upv.edu.mx

Abstract

Titanium and, in particular, its alloys are widely used in biomedical applications due to their favorable combination of mechanical properties, such as high strength, low density, low elastic modulus, and excellent biocompatibility. In this study, novel titanium-based alloys were developed using powder metallurgy techniques. The chemical composition of the studied alloys was 93%Ti-7%Fe, 90%Ti-7%Fe-3%Al, and 88%Ti-7%Fe-5%Cr. The metallic powders were processed in a planetary mill, uniaxially compacted, and subsequently sintered at 1300 °C during 2 h under an inert atmosphere. The primary objective was to evaluate the corrosion behavior of these alloys in simulated body fluid solutions, as well as to determine some of the properties, such as the relative density, microhardness, and elastic modulus. The resulting microstructures were homogeneous, with micrometer-scale grain sizes and the formation of intermetallic precipitates generated during sintering. Mechanical tests revealed that the Ti-Fe-Cr alloy exhibited the highest microhardness and Young's modulus values, followed by Ti-Fe and Ti-Fe-Al. These results confirm a strong correlation between hardness and stiffness, showing that Cr enhances mechanical and elastic properties, while Al reduces them. Corrosion tests demonstrated that the alloys possess high resistance and stability in physiological environments, with a low current density, minimal mass loss, and strong performance even under prolonged exposure to acidic conditions.

Keywords: titanium alloys; biomedical implants; powder metallurgy; electrochemical corrosion testing; biomedical-grade titanium alloys

check for updates

Received: 20 August 2025
Revised: 8 September 2025
Accepted: 28 September 2025
Published: 11 October 2025

Citation: Rodríguez-Escobedo, K.I.; Pech-Rodríguez, W.J.; Bedolla-Valdez, Z.I.; Calles-Arriaga, C.A.; Miranda-Hernández, J.G.; Rocha-Rangel, E. Ti-Fe-Based Alloys Modified with Al and Cr for Next-Generation Biomedical Implants. *Eng* **2025**, *6*, 273. https://doi.org/10.3390/eng6100273

Copyright: © 2025 by the authors. Licensee MDPI, Basel, Switzerland. This article is an open access article distributed under the terms and conditions of the Creative Commons Attribution (CC BY) license (https://creativecommons.org/licenses/by/4.0/).

1. Introduction

Titanium alloys are widely recognized for their high mechanical strength, durability, excellent corrosion resistance, and remarkable biocompatibility, making them materials of great interest in the field of biomedical engineering. Its unique combination of mechanical properties, including high strength, low density, and low modulus of elasticity, and chemical properties (such as its passivity to physiological media) has driven its use in a wide variety

of clinical applications [1–6]. However, despite their widespread use, challenges remain in optimizing their properties to achieve better performance under physiological conditions. The interrelationship between mechanical and chemical properties and biological behavior is crucial for the design of new alloys that can overcome the limitations of currently available materials [7]. Studies on Ti-Fe alloys have shown that the addition of iron does not compromise their biocompatibility, since it does not induce severe immunological reactions nor does it present appreciable toxic effects [8]. In this context, β-titanium alloys, such as Ti-25Nb-5Fe and Ti-40Nb, have been synthesized by powder metallurgy techniques. The results indicated significant improvements in their physical, electrochemical, and tribo-electrochemical properties, especially when the sintering time was increased and the particle size of the iron used was reduced [9]. In addition, several ternary Ti-5Fe-xAl alloys have been developed using elemental powder metallurgy through the economic method of pressing and sintering. The progressive incorporation of spherical aluminum powder did not significantly affect the compressibility of the material, but it did alter the thermodynamics of the sintering process. After this treatment, an increase in relative density was observed, reaching a maximum value of 98.7% with 3% by weight of Al, subsequently decreasing to 96.1% for the Ti-5Fe-6Al composition [10]. On the other hand, recent studies have evaluated the mechanical and corrosion properties of the Ti-xMo-2Fe alloy, the results of which showed a corrosion resistance superior to that of the Ti-6Al-4V ELI alloy. The BCC structure of Ti-xMo-2Fe enabled it to achieve higher compressive strength and elongation values. In tests with 3.5% NaCl solution, a 15.6% increase in corrosion potential (E_{corr}) and up to a sevenfold decrease in corrosion current density (I_{corr}) were reported, indicating a higher passivation capacity. In a 5 M HCl solution, the mass loss was only one-seventh of that observed for Ti-6Al-4V ELI, confirming its excellent chemical stability [11]. The commercial alloy Ti-6Al-4V, belonging to the α + β group, is the most widely used due to its good combination of strength and ductility. However, it has been reported that the addition of 0.55% Fe further improves its cyclic loading behavior by reducing fatigue softening and limiting crack propagation [12]. In order to modify the thermal expansion properties of titanium, Gd-Fe intermetallic compounds have been used, which, due to their low coefficient of thermal expansion, act as expansion-inhibiting agents upon reacting in situ with the Ti matrix. This combination generates a synergistic effect that significantly improves physical properties, especially dimensional stability [13]. On the other hand, the Ti-5Al-3V-6Cu (Ti536) alloy has demonstrated suitability for load-bearing applications in medical devices. Electrochemical tests revealed that Cu content has a minimal effect on corrosion current density, although it has a slight influence on stability, defect density, and corrosion behavior [14]. Ti-xAl-yCu alloys produced by powder metallurgy have been shown to exhibit better mechanical performance compared with their cast counterparts, making them a promising alternative for the manufacture of medical and dental implants of higher quality and lower cost [15]. A porous Ti-26Nb-6Mo-1.5Sn alloy has been developed by a combination of mechanical alloying and sintering for biomedical applications. This alloy was characterized by nanoindentation and tribology tests, showing favorable mechanical properties achieved thanks to the microstructural refinement derived from the mechanical alloying process [16]. On the other hand, biodegradable Fe-Mn alloys have been processed by powder metallurgy, obtaining alloys with high chemical and mechanical properties due to the type of processing carried out from powders [17]. Finally, Sur et al. address the rapid identification of corrosion-resistant alloys based on combinations of Al and Cr, providing a solid foundation for the design of alloys with improved properties [18]. Thus, the present work aims to analyze the effect of aluminum (Al) and chromium (Cr) additions in Ti-Fe base alloys synthesized by powder metallurgy

by evaluating their influence on the microstructure, phase formation, and the resulting mechanical and chemical properties.

2. Materials and Methods

The powders used for the preparation of the biomaterials were titanium (1 μm, 99.5%), iron (4 μm, 99.8%), aluminum (1–2 μm, 99%), and chromium (3 μm, 99%), all of them manufactured by SkySpring Nanomaterials, Inc., (Houston, TX, USA). The chemical compositions of the fabricated alloys were 93%Ti-7%Fe, 90%Ti-7%Fe-3%Al, and 88%Ti-7%Fe-5%Cr. The grinding of the initial metal powders was carried out in a planetary type ball mill at 300 rpm for 6 h; during this stage, zirconia spherical grinding elements with diameters of 3 mm were used, the grinding was dry performed, and 1 mL of isopropyl alcohol was added as a control agent. The powder-to-ball weight ratio was 1:10. The grinding vessel is made of stainless steel and has a capacity of 250 mL. From the powders obtained from the milling, cylindrical pellets of 1 cm in diameter by 1 cm in height were manufactured by uniaxial pressing, using a tool-grade steel die and pressures of 300 kg/cm^2. The sintering of the pellets was carried out in an electric furnace at a temperature of 1350 °C for 2 h. The atmosphere inside the furnace was argon and the heating ramp followed was 10 °C/min. At the end of the cycle, the furnace was turned off and the samples were left to cool inside the furnace. After sintering, physical characterization of the composites was carried out, and density was obtained from the individual measurement of three samples per alloy, determining for each of them the diameter, height, and weight. Following the milling stage, the particle size distribution was determined using a Mastersizer 2000, (Worcestershire, UK). The ultrasonic method was used to determine Young's modulus, following ASTM standards [19], using a Japanese-made Grindosonic A-360, (Heverlee, Bélgica, Belgium). The microhardness was evaluated in accordance with ASTM E384-16 [20]. In this case, twelve measurements were made at different points of the sample and the average value of the indentations is shown; these measurements were made with a microhardness tester (Wilson Instruments Model S400, Bluff, IL, USA). The analysis of the phases presents in the powders resulting from milling was carried out with a Bruker diffractometer, model D8 Advance, Billerica, MA, USA. The microstructural characteristics of the composite materials were observed by SEM using JEOL equipment (Akishima, Tokyo, Japan), model JSM-6480LV. The analysis was performed using an accelerating voltage of 20 kV, Backscattered Electron Signal, and high vacuum mode. The elemental composition and mapping distribution were determined by an EDS detector (Bruker 133eV) incorporated in a SEM JEOL 6400. The electrochemical characterization of titanium alloys was carried out using an ACM Instruments potentiostat–galvanostat, model Gill AC, (Cumbria, LA11 6HH, UK). With this equipment, electrochemical impedance spectroscopy (EIS) and potentiodynamic polarization tests were performed using a three-electrode cell. Hanks' Balanced Salt Solution (HBS) from Biowest (Nuaillé, France) was used to perform these tests. The corrosion rate of the samples was calculated using the gravimetric technique and the following Formula (1) [21]:

$$Vcorr = mi - mf/\rho At \quad (1)$$

where $Vcorr$ is the corrosion rate, mi is the initial mass, mf is the final mass, ρ is the density of the material, A is the exposure area, and t is the exposure time.

3. Results

3.1. Particle Size

The graphs corresponding to the particle size distribution for each of the study alloys are presented in Figure 1, where the average diameter of the samples analyzed on three

occasions is shown, as well as the standard deviation obtained. Thus, for the Ti-Fe alloy, a diameter corresponding to 50% accumulation of approximately 5.13 µm and a mean diameter of 5.267 µm were determined, with a size distribution ranging from 1 to 30 µm. In the case of the Ti-Fe-Al alloy, the cumulative diameter at 50% was 7.54 µm, with a mean of 7.428 µm. Finally, the Ti-Fe-Cr alloy presented a cumulative diameter at 50% of 6.09 µm and an average of 7.80 µm. In these last two alloys, the particle size ranged from 1 to just over 50 µm. The broad particle size distribution observed in the three alloys facilitates optimal packing during compaction, thereby increasing interparticle contact points and consequently enhancing the sintering process [22].

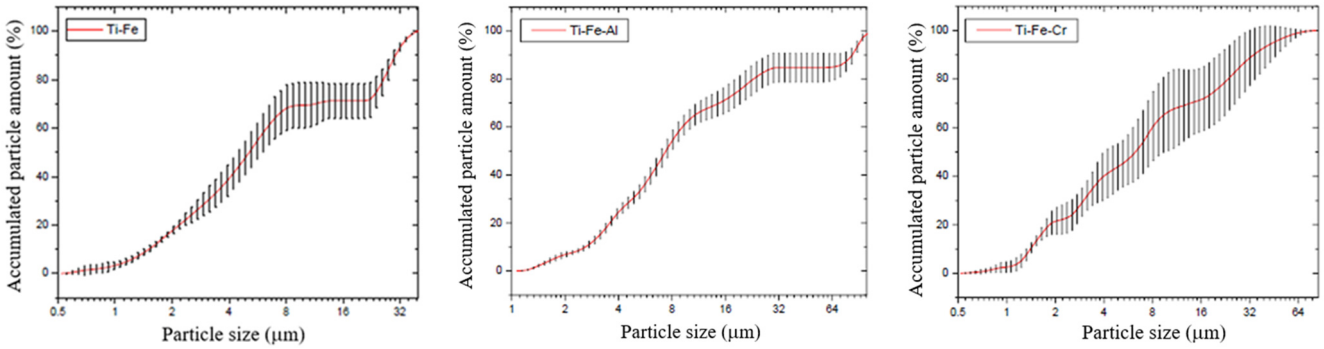


Figure 1. Particle size distribution in Ti-Fe, Ti-Fe-Al, and Ti-Fe-Cr alloys.

3.2. Powder Morphology

The microstructures of the powdered samples were observed by scanning electron microscopy (SEM). This analysis made it possible to examine in detail the morphology of the grains before the sintering process, evaluating their shape, size, and distribution. The corresponding micrographs are shown in Figure 2. In the images presented, the white and gray shades correspond to the alloy powders, while the black background color represents the surface on which the alloy powders were deposited. These images clearly show the agglomeration of the powders due to the milling process. Although this process reduces particle size, the metals are laminated and thus joined during this stage, resulting in the large sizes observed in Figure 1. This condition may be advantageous, as the alloy formation is initiated during the milling stage or, at least, the metal powders are activated to facilitate alloy generation during sintering. It is also observed that the morphology of the powders tends to be spherical or granular, which is due to the type of milling process to which they were subjected. The images show very fine particles measuring approximately 1 micron. However, in the case of agglomerates, these can reach sizes of up to 10 microns.

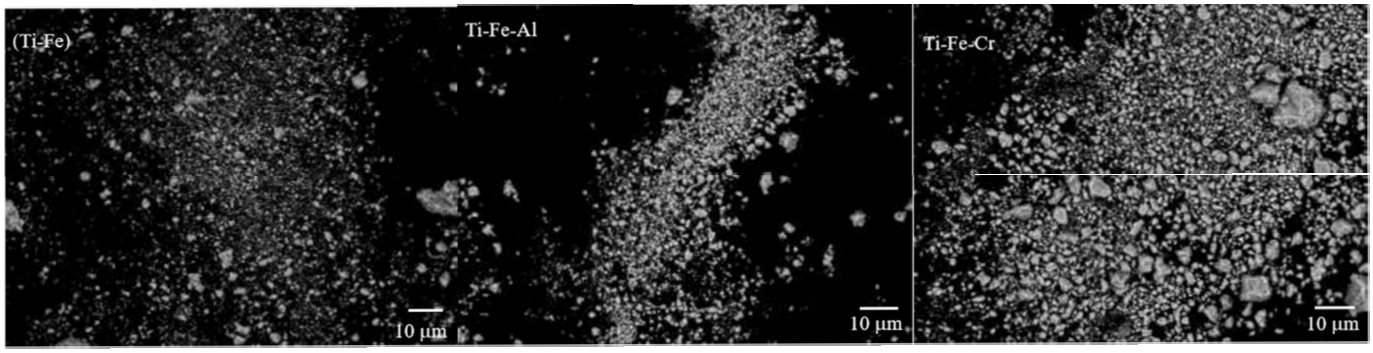


Figure 2. Images of the powders resulting from the milling stage of the three alloys.

3.3. Crystalline Phases in Powders

The powders corresponding to the three titanium alloys were analyzed by X-ray diffraction in order to identify the crystallographic planes present and to determine the type of crystalline structure in each sample. Figure 3a shows the diffractogram obtained for the Ti-Fe alloy. It identifies diffraction peaks at 2-theta angles of 35.1°, 38.4°, 40.2°, 53.1°, 63.3°, 70.6°, and 76.0°, corresponding to the (100), (002), (101), (102), (110), (103), and (112) planes, respectively, which correspond to the compact hexagonal phase associated with titanium. In addition, at 2-theta angles of 44.7°, 65.0°, and 82.3°, there are three peaks corresponding to the (110), (200), and (221) planes, which indicate the formation of body-centered cubic phases (BCCs), attributable to the presence of iron in the alloy. Figure 3b shows the diffractogram corresponding to the Ti-Fe-Al alloy. Diffraction peaks were identified at the 2-theta angles of the 35.1° plane (100), 38.4° plane (002), 40.2° plane (101), 53.1° plane (102), 63.3° plane (110), 70.6° plane (103), and 76.0° plane (112), which correspond to compact hexagonal phases, associated to the titanium. On the other hand, peaks at 2-theta angles of the 44.7° plane (110), 65.0° plane (200), and 82.3° plane (221) were observed, indicating the presence of body-centered cubic phases, attributable to the iron contained in the alloy. Additionally, peaks were detected in the 2-theta angles of the 44.7° plane (200), 65.1° plane (220), and 78.2° plane (311), which evidence the formation of face-centered cubic phases (FCCs), corresponding to the aluminum present in the composition. Figure 3c shows the diffractogram corresponding to the Ti-Fe-Cr alloy. In this pattern, the same peaks corresponding to Ti and Fe as in the patterns of Figure 3a,b were identified. Furthermore, diffraction peaks at 2-theta angles of 44.4°, 64.6°, 81.7°, and 98.9°, corresponding to the (110), (200), (221), and (220) planes, respectively, indicate the presence of body-centered cubic phases associated with the chromium in the alloy. These analyses confirm the presence of metallic elements in each of the alloys after the milling stage.

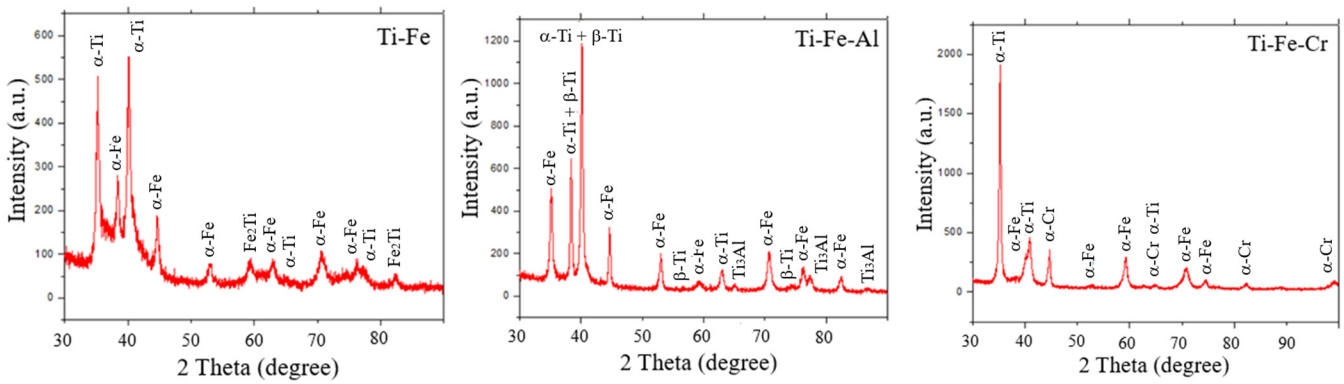


Figure 3. Diffraction patterns performed on the powders after the milling stage. Here there are the presentation of the different crystalline phases present in the milled powders, (**a**) Ti-Fe, (**b**) Ti-Fe-Al, (**c**) Ti-Fe-Cr.

3.4. Density

For each of the alloys studied, the actual density was calculated by direct measurements. These data made it possible to calculate the relative density of each sample, based on its corresponding theoretical density. The relative density of each sample was as follows: Ti-Fe—74%, Ti-Fe-Al—77%, and Ti-Fe-Cr—79%. The alloy with the highest density was the one with chromium added, while the original Ti-Fe alloy was the one with the lowest density value. With these density values, it is estimated that the porosity in the Ti-Fe, Ti-Fe-Al, and Ti-Fe-Cr alloys was 26, 23, and 21%, respectively. Compared to the porosity

reported for cortical bone, which ranges from 5 to 30%, it is within the expected range for a bone [23,24].

3.5. Microstructure

Figure 4 shows images taken with the aid of an optical microscope at 10× magnification of the microstructure of the three alloys. The images show the presence of porosity in the alloys, whose values agree with the porosity measured in the previous section. The presence of this porosity, mechanically speaking, may not be optimal, because it is in the pores where the cracks have their origin. However, in a bone, the presence of porosity is important because it is precisely in these areas where the osseointegration of the material into the body begins to take place, with the pores being necessary for the growth of tissue in the alloy for its definitive incorporation into the body.

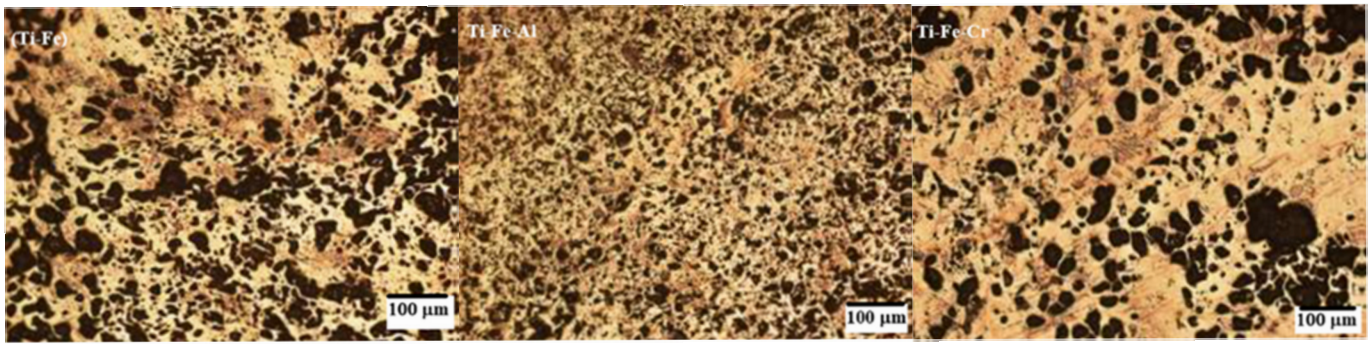
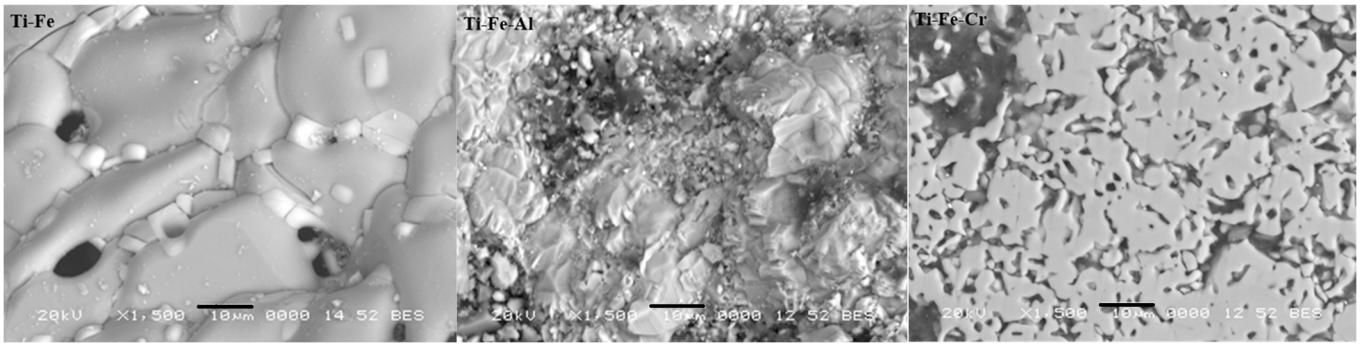


Figure 4. Microstructure of sintered alloys observed with optical microscopy. Here it is presented the microstructure of three alloys (Ti-Fe, Ti-Fe-Al, and Ti-Fe-Cr), highlighting the grain size, the presence and location of precipitates, as well as the phases or intermetallic compounds formed.

Scanning electron microscope images of the microstructure of the three sintered alloys are shown in Figure 5. Figure 5a, which corresponds to the Ti-Fe alloy, shows the presence of some precipitates, which are mainly located in intergranular zones. The grain size here is just over 10 microns, while that of the precipitates is about 2 microns. According to the binary phase diagram of the Ti-Fe system [25] for the composition of this alloy, the matrix of the alloy consists of a mixture of α-Ti and α-Fe phases, while the precipitates correspond to the Fe_2Ti intermetallic compound. For the Ti-Fe-Al alloy shown in Figure 5b, as well as in the case of the Ti-Fe alloy, the formation of some precipitates can be observed, which are located in intragranular zones; the grain size of the matrix is much larger and greater than 10 microns, while that of the precipitates is between 3 and 4 microns. According to the ternary diagram of the Ti-Fe-Al system and the composition of the alloy studied [25], the matrix is a mixture of α and β phases of titanium, and the precipitates formed most likely correspond to the Ti_3Al intermetallic. In the microstructure of Figure 5c, corresponding to the Ti-Fe-Cr alloy, the formation of precipitates is not observed; in this case, a homogeneous microstructure is observed in morphology with the formation of porosity, where the grain size varies from a few microns to more than 10 microns. According to the ternary phase diagram of the Ti-Fe-Cr system and to the composition of this alloy [26], the structure of the alloy is predominantly body-centered cubic. Due to the composition of the alloy in this case, no precipitates of any intermetallic compound are formed, as was the case with the two alloys shown above.



(**a**) (**b**) (**c**)

Figure 5. Microstructure of the sintered alloys observed by scanning electron microscopy. The figure presents the presence of intermetallic and porosity in the titanium alloys. (**a**) Ti-Fe, (**b**) Ti-Fe-Al, (**c**) Ti-Fe-Cr.

3.6. Mappings

Figure 6 shows mappings of the elements present in each of the alloys manufactured. For each alloy, the figure presents a microstructure image of the area where the mapping was performed, a general mapping with all the metallic elements present in each alloy, and individual images showing the distribution of each metal in the alloy. In general, there is a homogeneous distribution of the alloying elements Fe, Al, and Cr in a Ti matrix. The homogeneous distribution of the metals in the respective alloy is an indication of the formation of the desired alloy in each case. It is worth mentioning that the mappings were performed on images magnified 500 times in order to cover a large area of each alloy.

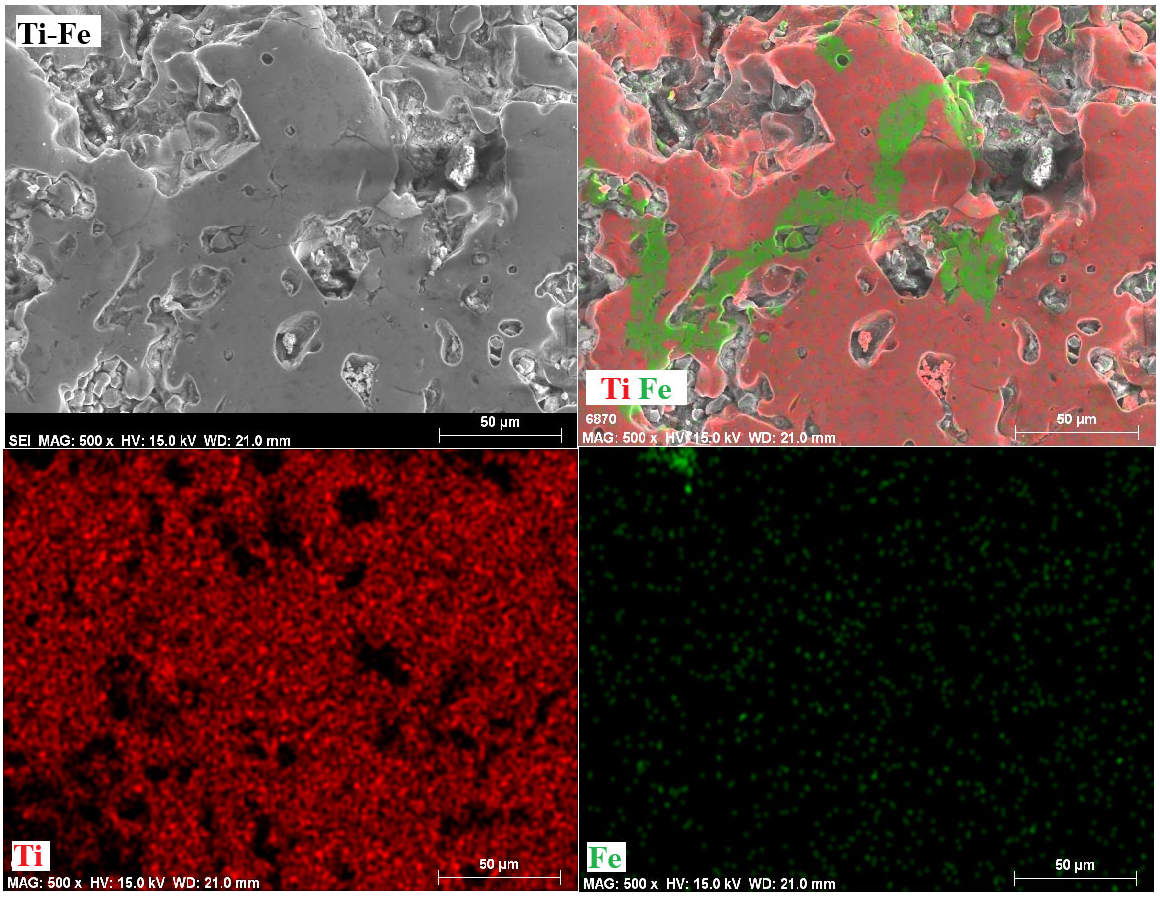


Figure 6. *Cont.*

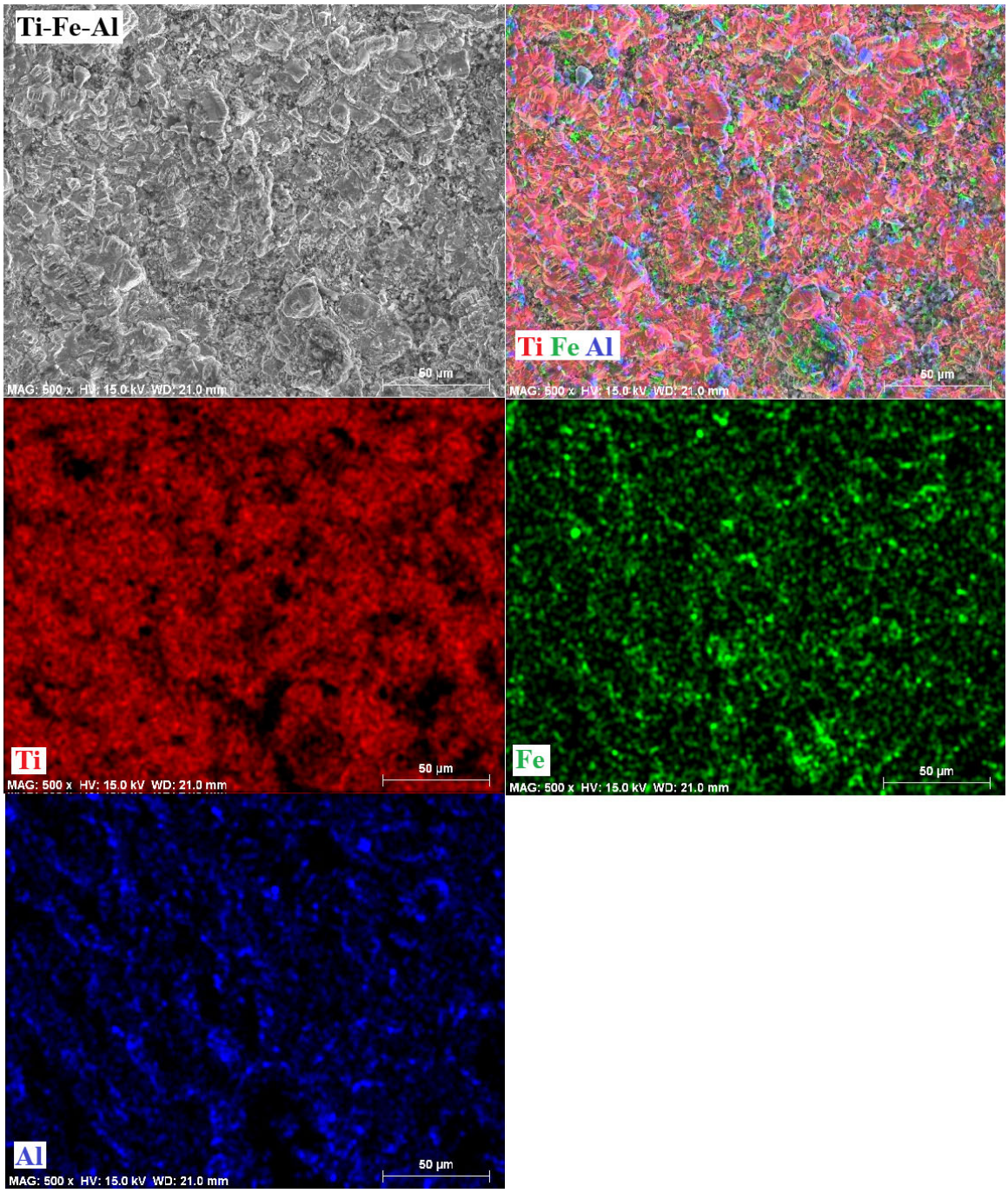


Figure 6. *Cont.*

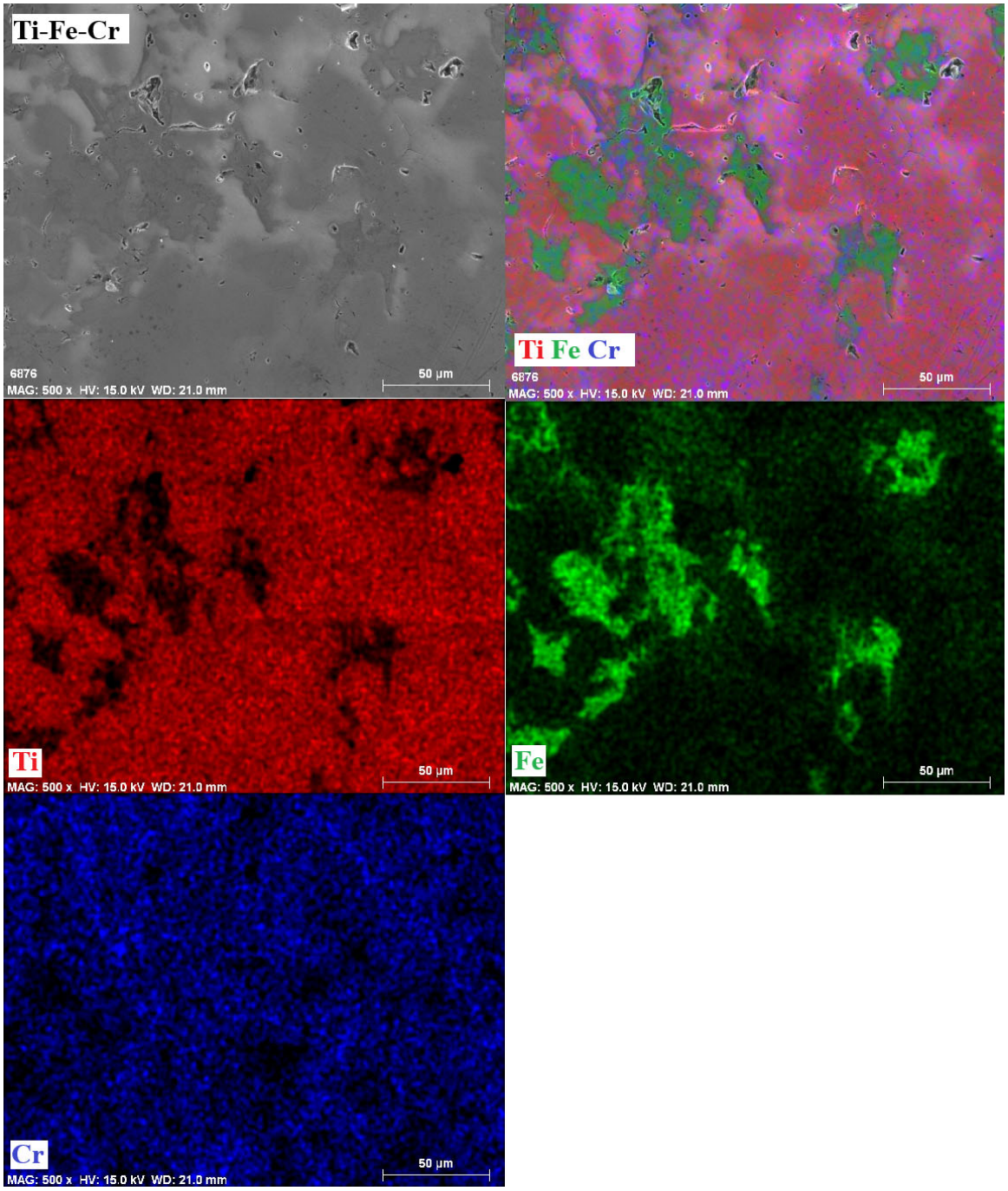


Figure 6. Mappings of sintered alloys.

3.7. Mechanical Properties

3.7.1. Microhardness

Figure 7 shows the microhardness values obtained for each of the alloys, together with their respective standard deviations. It is observed that the Ti-Fe-Cr alloy presents the highest microhardness value, far exceeding the other two compositions. This behavior is attributed to the incorporation of chromium into the titanium crystal lattice, where it forms a substitutional solid solution. The difference in atomic size between Cr and Ti causes distortions in the lattice, hindering the movement of dislocations and, therefore, increasing the hardness of the material. In contrast, the Ti-Fe-Al alloy exhibited the lowest microhardness, which can be attributed to the fact that aluminum, being a relatively soft metal, does not induce significant distortion in the crystal lattice. Although it can form

the intermetallic Ti_3Al, its hardening effect is limited, as it does not favor a high density of dislocations or significant obstruction to their movement. The Ti-Fe alloy, in turn, exhibited an intermediate microhardness value, which is explained by the formation of intermetallic phases such as Fe_2Ti, as well as by moderate distortion of the titanium network, which partially contributes to mechanical reinforcement. It should be noted that the reported value of microhardness for cortical bone is in the range of 50 to 70 HV [27,28]. Compared to the values obtained for the alloys synthesized in this work, the bone presents a considerably lower hardness, suggesting that, from a mechanical point of view, the alloys developed are suitable for applications where higher resistance to deformation is required.

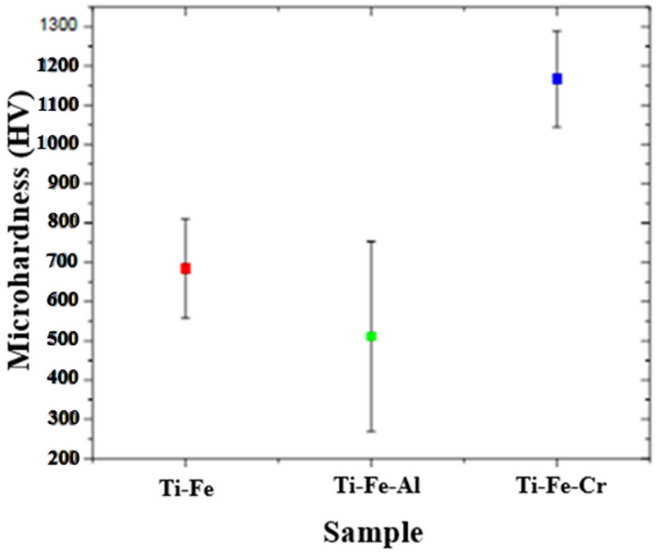


Figure 7. Microhardness of the three study alloys.

3.7.2. Elastic Modulus

Figure 8 shows the values of the elastic modulus of each alloy, as well as their respective standard deviations. Likewise, this figure shows the theoretical elastic moduli of each alloy. In the case of the Ti-Fe-Cr alloy, it has the highest Young's modulus both theoretically (~130 GPa) and experimentally. As can be seen, the experimental value is quite close to the theoretical value, with a relatively short error bar, which suggest good structural stiffness, that can be attributed to a homogeneous microstructure. The high modulus is related to the presence of Cr, which improves the stiffness by distorting the crystal lattice. In the case of the Ti-Fe-Al alloy, it is the one with the lowest theoretical modulus (~115 GPa). Likewise, the experimental modulus was also low and with a wide error bar, which indicates variability in the measurements or microstructural heterogeneity. Al reduces the stiffness of the material due to its soft nature and low capacity to reinforce the Ti crystal lattice. The Ti-Fe alloy presents an intermediate theoretical modulus, and the experimental value is the lowest of the three (~110 GPa) and presents the greatest dispersion of results. The high error bar suggests variability in the internal structure (possibly due to porosity or inhomogeneous phases). Although it forms hard intermetallic phases such as Fe_2Ti, it was not enough to reach the theoretical modulus. The differences between theoretical and experimental modulus can be attributed to the presence of porosity in the alloys.

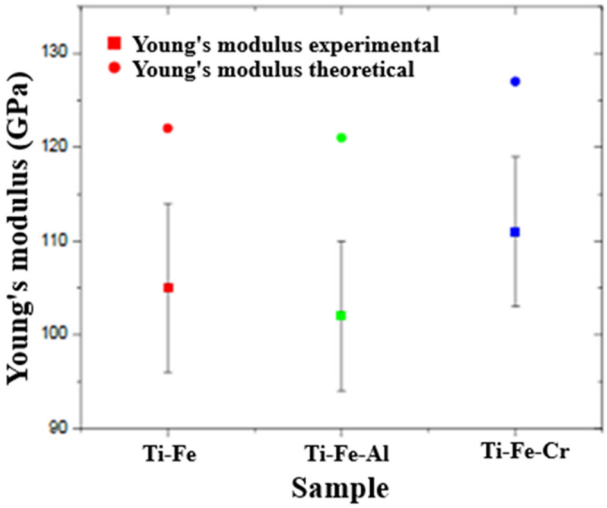


Figure 8. Elastic modulus of the three alloys under study.

3.8. Corrosion Test

Figure 9 shows the polarization curves obtained by electrochemical spectroscopy as part of the corrosion test. In the graph, the vertical axis corresponds to the potential (mV vs. RHE—Reversible Hydrogen Electrode) and the horizontal axis to the current density in logarithmic scale (Log [A cm^{-2}]). A lower corrosion current density (I_{corr}) indicates a lower corrosion rate. The figure shows that sample Ti-Fe had the lowest I_{corr}, indicating that it was the most resistant to corrosion. On the other hand, Ti-Fe-Cr exhibited the highest E_{corr}, suggesting a higher resistance to electrochemical degradation.

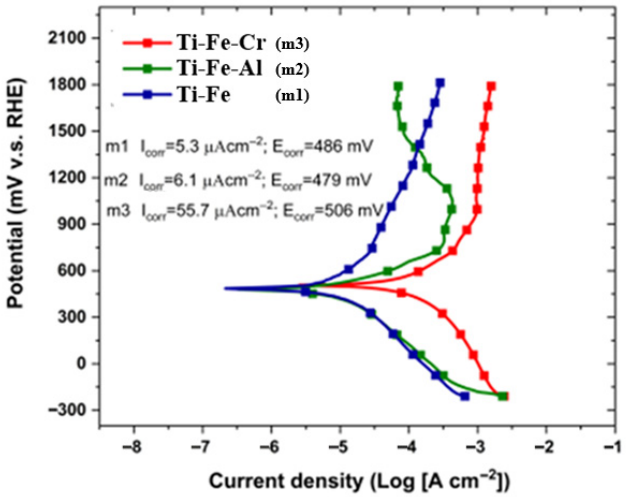


Figure 9. Polarization curves obtained by electrochemical spectroscopy in the alloys under study.

3.9. Corrosion by Chemical Agent

Corrosion tests were carried out using a chemical agent known as Kroll's agent, composed of 92% water (H_2O), 6% nitric acid (HNO_3), and 2% hydrofluoric acid (HF). This reagent is widely used to evaluate the chemical resistance of metallic materials, particularly in studies related to corrosion. The samples were submerged for an extended period in order to evaluate mass loss as an indicator of their corrosion resistance. To ensure detailed monitoring, periodic measurements of the mass of the samples were taken every 24 h. This procedure made it possible to identify trends in the behavior of materials when subjected to sustained chemical attack, providing key information about their durability and stability

under aggressive conditions. Figure 10 shows a graph illustrating the behavior of the samples during the test.

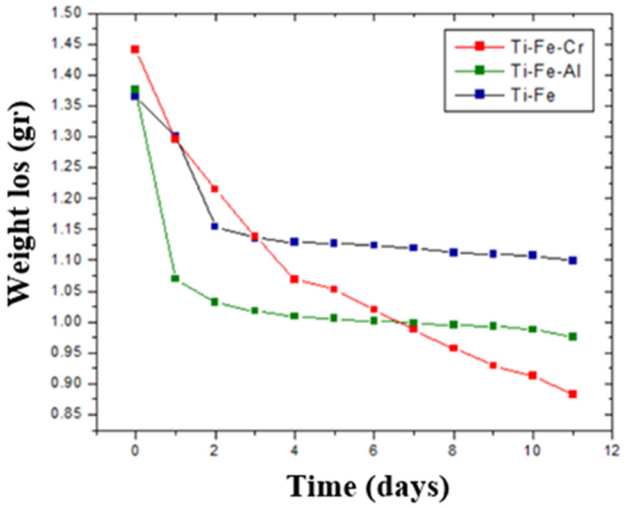


Figure 10. Chemical attack with Kroll agent.

Table 1 summarizes the five electrochemical parameters of the tested samples extracted from the polarization curves, including polarization resistance (R_p) and the anodic and cathodic slopes (β_a and β_c). Among them, Ti-Fe exhibits the lowest corrosion current density (I_{corr}) along with the highest R_p, further confirming its outstanding corrosion resistance. This result is consistent with the behavior observed in Figure 10, where Ti-Fe has the smallest weight loss after 11 days of exposure to Kroll agent. Additionally, it should be noted that this sample has a lower decay slope in comparison with Ti-Fe-Cr. Although the incorporation of Cr has been reported to enhance corrosion resistance, the key factor in this study was the sample morphology. For example, from Figure 5a, it can be observed that Ti-Fe has an entangled structure with small pores, whereas Ti-Fe-Cr displays a more porous structure that facilitates electrolyte diffusion during corrosion testing.

Table 1. Electrochemical parameters extracted from the polarization curves.

Sample	E_{corr} (mV)	I_{corr} ($\mu A \cdot cm^{-2}$)	β_a (V)	β_c (V)	R_p ($\Omega \cdot cm^{-2}$)
M1	486	5.3	0.262	0.130	7127.7
M2	479	6.1	0.122	0.163	4973.3
M3	506	55.7	0.118	0.100	422.5

From these results, the corrosion rate was 68.24, 86.38, and 115.92 mm/year for the Ti-Fe, Ti-Fe-Al, and Ti-Fe-Cr alloys, respectively. These values corroborate the electrochemical polarization results, indicating that the Ti-Fe alloy exhibits the highest corrosion resistance, whereas the Ti-Fe-Cr alloy shows the lowest 17. The curves flatten after about 6 days for the Ti-Fe and Ti-Fe-Al alloys, suggesting passivation. In the study by Ribeiro et al. [29], the presence of the alpha phase in the microstructure of a titanium-based alloy is analyzed. This alpha phase affects the chemical and electrochemical behavior of the alloy when exposed to the Kroll reagent, suggesting a protective capacity due to a surface oxide formed on it. This situation helps to understand the passivation observed in the aforementioned alloys. However, the weight loss rates of the alloys are negligible, indicating that all three exhibit high resistance to attack by solutions with chemical compositions similar to that of human body fluids.

4. Conclusions

This work evaluates Ti-Fe-based alloys for biomedical use, focusing on their microstructure, mechanical behavior, and corrosion resistance. The influence of alloying elements on hardness, elasticity, and stability in aggressive environments was analyzed to establish their potential for biocompatible applications. The following conclusions were thus reached:

- Images obtained using optical microscopy reveal a microstructure with significant porosity, which is relevant for biomedical applications, as it can promote biocompatibility through cell adhesion to the host. In addition, a homogeneous alloy with fine grains was observed, suggesting effective control in the synthesis and sintering processes.
- The phases present in the alloys were as follows. For the Ti-Fe alloy, the matrix consists of a mixture of α-Ti and α-Fe phases, with the formation of Fe_2Ti intermetallic precipitates. The Ti-Fe-Al alloy has a matrix with a mixture of α and β phases of titanium and precipitates of the intermetallic Ti_3Al. In contrast, the Ti-Fe-Cr alloy has a predominantly body-centered cubic structure without the formation of intermetallic precipitates.
- The data obtained in the microhardness tests show that the Ti-Fe-Cr alloy presented the highest resistance to localized deformation, followed by Ti-Fe and, finally, Ti-Fe-Al. This behavior indicates a direct relationship between the composition of the alloys and their mechanical properties.
- In the Young's modulus measurements, it was observed that the Ti-Fe-Cr alloy also had the highest values, followed by Ti-Fe and Ti-Fe-Al. This finding is consistent with microhardness data, reinforcing the correlation between hardness and stiffness in the evaluated alloys. The presence of Cr significantly improves elastic properties, while Al tends to decrease them.
- Corrosion tests showed electrochemical potential values between 480 and 520 mV, indicating remarkable resistance to corrosive environments. In addition, the recorded current density values reflect a low tendency to corrosion, confirming that the alloys exhibit good stability in chemically aggressive conditions.
- Despite prolonged exposure to Kroll's reagent, the samples showed minimal mass loss, highlighting their stability in acidic environments.
- The Ti-Fe-Cr alloy emerges as the most advantageous alternative, as it exhibits the highest values of microhardness, Young's modulus, and relative density, thereby ensuring superior mechanical performance compared to the other alloys. Despite presenting the highest corrosion rate, the measured corrosion potentials confirm that, similar to the other systems, it maintains a high degree of chemical stability.

Author Contributions: Conceptualization, K.I.R.-E., W.J.P.-R. and E.R.-R.; methodology, K.I.R.-E., W.J.P.-R., Z.I.B.-V. and J.G.M.-H.; software, C.A.C.-A.; validation, K.I.R.-E., W.J.P.-R. and E.R.-R.; formal analysis, K.I.R.-E., W.J.P.-R. and E.R.-R.; investigation, K.I.R.-E., Z.I.B.-V. and J.G.M.-H.; resources, E.R.-R.; data curation, K.I.R.-E., Z.I.B.-V. and J.G.M.-H.; writing—original draft preparation, K.I.R.-E.; writing—review and editing, W.J.P.-R., C.A.C.-A. and E.R.-R.; visualization, E.R.-R.; supervision, E.R.-R.; project administration, K.I.R.-E., W.J.P.-R., C.A.C.-A. and E.R.-R.; funding acquisition, Z.I.B.-V., J.G.M.-H. and E.R.-R. All authors have read and agreed to the published version of the manuscript.

Funding: This research received no external funding.

Informed Consent Statement: Not applicable.

Data Availability Statement: The original contributions presented in this study are included in the article. Further inquiries can be directed to the corresponding author.

Acknowledgments: Katia Itzel Rodríguez Escobedo would like to express their appreciation to SECIHTI for the grant to carry out her Master's degree studies. The authors would like to thank Rody Oswaldo Mendez Villarreal for the SEM images technical support.

Conflicts of Interest: The authors declare no conflicts of interest.

Abbreviations

The following abbreviations are used in this manuscript:

E_{corr}	Corrosion potential
I_{corr}	Corrosion current density
SEM	Scanning electron microscopy
HV	Hardness Vickers
RHE	Reversible Hydrogen Electrode

References

1. Bandyopadhyay, A.; Mitra, I.; Goodman, S.B.; Kumar, M.; Bose, S. Improving biocompatibility for next generation of metallic implants. *Prog. Mater. Sci.* **2023**, *133*, 101053. [CrossRef]
2. Chen, L.Y.; Cui, Y.W.; Zhang, L.C. Recent development in beta titanium alloys for biomedical applications. *Metals* **2020**, *10*, 1139. [CrossRef]
3. El-Bassyouni, G.T.; Mouneir, S.M.; El-Shamy, A.M. Advances in surface modifications of titanium and its alloys: Implications for biomedical and pharmaceutical applications. *Multiscale Multidiscip. Model. Exp. Des.* **2025**, *8*, 1–47. [CrossRef]
4. Kaur, M.; Singh, K. Review on Titanium and Titanium Based Alloys as Biomaterials for Orthopaedic Applications. *Mater. Sci. Eng. C Mater. Biol. Appl.* **2019**, *102*, 844–862. [CrossRef] [PubMed]
5. Lu, J.; Zhao, Y.; Niu, H.; Zhang, Y.; Du, Y.; Zhang, W.; Huo, W. Electrochemical corrosion behavior and elasticity properties of Ti-6Al-xFe alloys for biomedical applications. *Mater. Sci. Eng. C* **2016**, *62*, 36–44. [CrossRef] [PubMed]
6. Trevisan, F.; Calignano, F.; Aversa, A.; Marchese, G.; Lombardi, M.; Biamino, S.; Ugues, D.; Manfredi, D. Additive manufac-turing of titanium alloys in the biomedical field: Processes, properties and applications. *J. Appl. Biomater. Funct. Mater.* **2018**, *16*, 57–67. [CrossRef]
7. Jawed, S.F.; Rabadia, C.D.; Khan, M.A.; Khan, S.J. Effect of alloying elements on the compressive mechanical properties of biomedical titanium alloys: A systematic review. *ACS Omega* **2022**, *7*, 29526–29542. [CrossRef]
8. Niu, J.; Guo, Y.; Li, K.; Liu, W.; Dan, Z.; Sun, Z.; Chang, H.; Zhou, L. Improved mechanical, bio-corrosion properties and in vitro cell responses of Ti-Fe alloys as candidate dental implants. *Mater. Sci. Eng. C* **2021**, *122*, 111917. [CrossRef] [PubMed]
9. Çaha, I.; Alves, A.; Chirico, C.; Pinto, A.; Tsipas, S.; Gordo, E.; Toptan, F. Corrosion and tribocorrosion behavior of Ti-40Nb and Ti-25Nb-5Fe alloys processed by powder metallurgy. *Metall. Mater. Trans. A* **2020**, *51*, 3256–3267. [CrossRef]
10. Alshammari, Y.; Manogar, B.; Raynova, S.; Yang, F.; Bolzoni, L. Behaviour of novel low-cost blended elemental Ti–5Fe-xAl alloys fabricated via powder metallurgy. *J. Mech. Behav. Biomed. Mater.* **2020**, *110*, 103865. [CrossRef]
11. Park, J.Y.; Lee, J.G.; Lee, Y.J.; Lee, D.G. Effect of molybdenum on the mechanical and corrosion properties of Ti-xMo-2Fe beta alloys. *J. Korean Inst. Met. Mater.* **2024**, *62*, 125–131. [CrossRef]
12. Sun, Y.; Qian, S.; Chang, H.; Duan, W.; Feng, L.; Li, F.; Zhou, L. Improved low cycle fatigue property of Ti–6Al–4V alloy by trace Fe addition. *J. Mater. Res. Technol.* **2024**, *30*, 8396–8408. [CrossRef]
13. Xia, F.; Yang, X.; Yan, Y.; Liang, M. Development of novel Gd-Fe/Ti composites with tunable thermal expansion property. *Mater. Res. Express* **2024**, *11*, 096514. [CrossRef]
14. Behjat, A.; Sanaei, S.; Mosallanejad, M.H.; Atapour, M.; Sheikholeslam, M.; Saboori, A.; Iuliano, L. A novel titanium alloy for load-bearing biomedical implants: Evaluating the antibacterial and biocompatibility of Ti536 produced via electron beam powder bed fusion additive manufacturing process. *Biomater. Adv.* **2024**, *157*, 213928. [CrossRef]
15. Bolzoni, L.; Yang, F. Development of Cu-bearing powder metallurgy Ti alloys for biomedical applications. *J. Mech. Behav. Biomed. Mater.* **2019**, *97*, 41–48. [CrossRef]
16. Pedram Sotoudeh Bagha, P.S.; Khakbiz, M.; Safaie, N.; Sheibani, S.; Ebrahimi-Barough, S. Effect of high energy ball milling on the properties of biodegradable nanostructured Fe-35 wt.%Mn alloy. *J. Alloys Comp.* **2018**, *768*, 166–175. [CrossRef]
17. Safaie, N.; Khakbiz, M.; Sheibani, S.; Bagha, P.S. Synthesizing of Nanostructured Fe-Mn Alloys by Mechanical Alloying Process. *Procedia Mater. Sci.* **2015**, *11*, 381–385. [CrossRef]
18. Sur, D.; Holcombe, E.F.; Blades, W.H.; Anber, E.A.; Foley, D.L.; DeCost, B.L.; Liu, J.; Hattrick-Simpers, J.; Sieradzki, K.; Joress, H.; et al. An experimental high-throughput to high-fidelity study towards discovering Al-Cr containing corrosion-resistant compositionally complex alloys. *High Entropy Alloys Mater.* **2023**, *1*, 336–353. [CrossRef]

19. *ASTM E1876-22*; Standard Test Method for Dynamic Young's Modulus, Shear Modulus, and Poisson's Ratio by Impulse Exci-tation of Vibration. ASTM International: West Conshohocken, PA, USA, 2022.
20. *ASTM E384-16*; Standard Test Method for Microindentation Hardness of Materials. ASTM International: West Conshohocken, PA, USA, 2016.
21. Malaret, F. Exact calculation of corrosion rates by the weight-loss method. *Exp. Results* **2022**, *3*, e13. [CrossRef]
22. Bai, Y.; Wagner, G.; Williams, C.B. Effect of Particle Size Distribution on Powder Packing and Sintering in Binder Jetting Additive Manufacturing of Metals. *J. Manuf. Sci. Eng.* **2017**, *139*, 081019–081024. [CrossRef]
23. Currey, J.D. *Bones: Structure and Mechanics*; Princeton University Press: Princeton, NJ, USA, 2022.
24. Dia, A.S.; Renaud, G.; Chappard, C.; Grimal, Q. Ultrasound imaging of cortical bone: Cortex geometry and measurement of porosity based on wave speed for bone remodeling estimation. *arXiv* **2025**, arXiv:2502.08824. [CrossRef]
25. Liang, Z.; Kattner, U.; Choudharry, K.; Tavazza, F.; Campbell, C. Thermodynamic assessments of Ti-Al, Ti-Fe, and Ti-Al-Fe systems with four-sublattice description of ordered body-centered cubic phase and density functional theory data. *J. Phase Equilib. Diffus.* **2024**, *45*, 732–756. [CrossRef]
26. Wang, S.; Wang, K.; Chen, G.; Li, Z.; Qin, Z.; Lu, X.; Li, C. Thermodynamic modeling of Ti-Fe-Cr ternary system. *Calphad* **2017**, *56*, 160–168. [CrossRef]
27. Li, S.; Wang, J.Z.; Yin, B.; Hu, Z.S.; Zhang, X.J.; Wu, W.; Liu, G.B.; Liu, Y.K.; Fu, L.; Zhang, Y.Z. Atlas of human skeleton hardness obtained using the micro-indentation technique. *Orthop. Surg.* **2021**, *13*, 1417–1422. [CrossRef] [PubMed]
28. Marin, E.; Lanzutti, A. Biomedical applications of titanium alloys: A comprehensive review. *Materials* **2024**, *17*, 114. [CrossRef] [PubMed]
29. Ribeiro, R.B.; Hein, L.R.d.O.; Robin, A. Influence of aged Ti-15V-3Cr-3Sn-3Al alloy microstructure on chemical and electrochemical behavior in the Kroll reagent for metallographic etching. *Prakt. Metallogr.* **2003**, *40*, 16–23. [CrossRef]

Disclaimer/Publisher's Note: The statements, opinions and data contained in all publications are solely those of the individual author(s) and contributor(s) and not of MDPI and/or the editor(s). MDPI and/or the editor(s) disclaim responsibility for any injury to people or property resulting from any ideas, methods, instructions or products referred to in the content.